# Photofragmentation of the Gas-Phase Lanthanum Isopropylcyclopentadienyl Complex: Computational Modeling vs Experiment

Yulun Han,[†] Qingguo Meng,[‡] Bakhtiyor Rasulev,[§] P. Stanley May,[†] Mary T. Berry,[†] and Dmitri S. Kilin*,[†,∥]

[†]Department of Chemistry, University of South Dakota, Vermillion, South Dakota 57069, United States
[‡]Shenyang Institute of Automation, Guangzhou, Chinese Academy of Sciences, Guangzhou 511458, China
[§]Center for Computationally Assisted Science and Technology, North Dakota State University, Fargo, North Dakota 58102, United States
[∥]Department of Chemistry and Biochemistry, North Dakota State University, Fargo, North Dakota 58108, United States

**S** *Supporting Information*

**ABSTRACT:** Photofragmentation of the lanthanum isopropylcyclopentadienyl complex, La(iCp), was explored through time-dependent excited-state molecular dynamics (TDESMD), excited-state molecular dynamics (ESMD), and thermal molecular dynamics (MD). Simulated mass spectra were extracted from *ab initio* molecular dynamics simulations through a new and simple method and compared to experimental photoionization time-of-flight (PI−TOF) mass spectra. The computational results indicate that the value of excitation energy and mechanism of excitation determine the dissociation process.
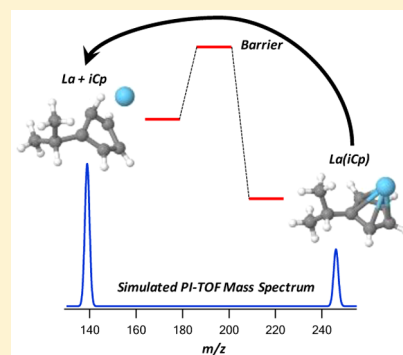
## 1. INTRODUCTION

As the size of transistors continues to shrink, it is important to replace the traditional gate oxide, $SiO_2$, with other high-$k$ dielectric constant materials, which could overcome current leakage. Lanthanide oxides have been investigated as alternatives to traditional $SiO_2$ gate dielectrics in metal-oxide-semiconductor field-effect transistors (MOSFETs) due to their large band gap,[1] high dielectric constant,[2] and relatively close lattice match to silicon.[3] In addition, lanthanide oxide thin films have other applications in protective coatings,[4] luminescent materials,[5] and waveguides.[6]

Lanthanide cyclopentadienyl (Cp) complexes have been frequently employed to prepare lanthanide oxide thin films by both metal−organic chemical vapor deposition (MOCVD) and atomic layer deposition (ALD) techniques.[7−9] Lanthanide cyclopentadienyl complexes could also be excellent candidates to fabricate lanthanide oxide thin films by photolytic laser-assisted metal−organic chemical vapor deposition (LCVD) with other oxidizing co-precursors, offering the advantage of high deposition speed and high purity.[10,11]

Experimentally, we and others have demonstrated that photoionization time-of-flight mass spectrometry (PI−TOF−MS) is a powerful tool for investigating the photofragmentation mechanisms of metal−organic precursors.[12−19] Theoretical and computational challenges of exploring the combined electronic and nuclear dynamics in the presence of laser field are due to the breakdown of the Born−Oppenheimer approximation.[20] For nonequilibrium states, the dynamics of the nuclei are coupled to the dynamics of the electronic state, going beyond the Born−Oppenheimer approximation, while electronic state dynamics is perturbed by electric field of laser.[21−28] The time evolution of coupled electronic and nuclear degrees of freedom can be explored by propagating the elements of the density matrix through the Liouville−von Neumann equation of motion.[25−27] Both trajectory surface hopping methods[23,28] and self-consistent potential methods[29,30] have been used to treat the coupling.

*Ab initio* molecular dynamics (AIMD) calculations have been used to describe the fragmentation of many systems. For instance, reactive molecular dynamics was used to study the decomposition of nanoscale carbon materials.[31,32] Isayev et al. performed AIMD simulations to study the decomposition of CL-20 (2,4,6,8,10,12-hexanitro-2,4,6,8,10,12-hexaazaisowurtzitane).[33] Greenfield et al. studied the photochemistry of pentaerythritol trinitrate chlorotetrazine (PetrinTzCl) through nonadiabatic excited molecular dynamics.[34] Grimme studied

the fragmentation of many molecules and simulated the electron impact mass spectra through molecular dynamics simulations.[35,36] Our group investigated the photofragmentation of lanthanide cyclopentadienyl complexes through time-dependent excited-state molecular dynamics (TDESMD).[37,38]

In this study, the photofragmentation of lanthanum isopropylcyclopentadienyl complex, La(iCp) was explored through time-dependent excited-state molecular dynamics (TDESMD), excited-state molecular dynamics (ESMD), and thermal molecular dynamics (MD), where the latter two provide well-understood methods as good reference points for comparison. Simulated mass spectra were extracted from *ab initio* molecular dynamics simulations through a new and simple method and directly compared with experimental photoionization time-of-flight (PI−TOF) mass spectra. The computational results indicate that the value of excitation energy and mechanism of excitation determine the dissociation process.

A fundamental premise, derived from the experimental work on similar complexes, is that the fragmentation products are dominated by reactions which occur within neutral complexes, yielding neutral fragments which are only detected by mass spectrometry following postfragmentation photoionization. That is, photoionization simply samples the fragmentation intermediates and final products and is not an integral part of the reaction mechanism.[38]

## 2. EXPERIMENTAL AND THEORETICAL METHODS

**2.1. PI−TOF Mass Spectrometry.** La(iCp)$_3$ (99.9%-La) was purchased from Strem Chemicals. Because La(iCp)$_3$ complexes are air and moisture sensitive, they were kept inside an argon-filled glovebox prior to use. The photofragmentation experiments were conducted using the photoionization time-of-flight mass spectrometer which is described in detail in previous work.[38] La(iCp)$_3$ complexes were loaded into the sample holder inside the glovebox. The sample holder was heated to ~120 °C to sublime the precursors. No carrier gas was used to transport the sample into the photoionization chamber. The gas-phase precursors effused into the time-of-flight mass spectrometer chamber due to the pressure difference between the sample holder (~10 mTorr) and the time-of-flight mass spectrometer chamber (~10$^{-4}$ mTorr). A photofragmentation wavelength of 266 nm (fourth harmonic of a Nd:YAG laser, 70 mJ pulse, $1.5 \times 10^9$ W/cm$^2$) was used.

**2.2. Computational Method.** All calculations were done in a basis set of Kohn−Sham orbitals computed in density functional theory (DFT) with the Perdew−Burke−Ernzerhof (PBE) functional under periodic boundary conditions in the basis of plane waves and using norm-conserving atomic pseudopotentials as implemented in the VASP software, providing a set of Kohn−Sham orbitals $\varphi_i^{KS}(\vec{r}, \{\vec{R}_I\})$ and energies $\varepsilon_i(\{\vec{R}_I\})$ for each nuclear configuration $\{\vec{R}_I\}$.[39−43] On the basis of the orbitals and energies, one can compute transition dipoles, $\vec{D}_{ij}$, oscillator strengths, $f_{ij}$, and absorption spectra. The ground state optimized geometry of the model is used as the starting point for MD, ESMD, and TDESMD simulations.

The conversion of the initial precursor into the final product fragments involves overcoming a barrier in the potential energy surface. The height of the barrier $E_a = U(R_B) − U(R_0)$ determines the minimum energy needed to activate fragmentation. A schematic diagram for a comparison of the three molecular dynamics methods is found in Figure 1. Each method
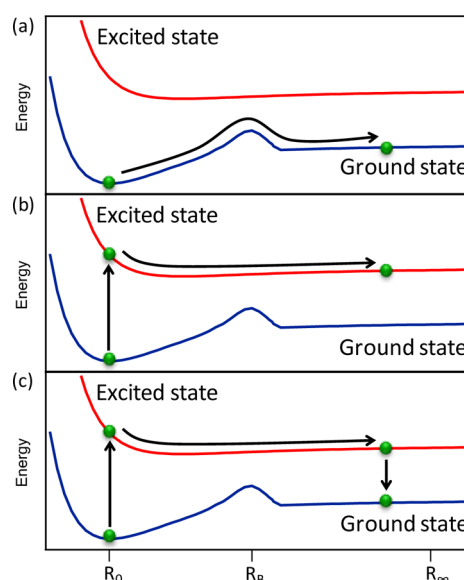


**Figure 1.** Schematic representation and comparison of the three computational methods used in this study: (a) MD, (b) ESMD, and (c) TDESMD. Each method describes a different path to overcome the dissociation barrier. Ground state MD includes thermal activation, ESMD includes one photoexcitation event, and TDESMD includes a sequence of excitation and de-excitation events, thus providing different photofragmentation trajectories.

describes a different path to overcome the dissociation barrier. These methods are introduced in the order of increasing complexity, from simple MD to complicated TDESMD. In MD simulations, the system remains in the electronic ground state, and its temperature is ramped linearly in time to achieve kinetic energy values comparable to those achieved in the TDESMD simulation. Technically, this is done by reassigning momentum to each nucleus at each time step. In ESMD, the electrons are promoted from ground state to a selected excited state configuration, in agreement with the excitation chosen for TDESMD simulations. ESMD is a limiting case of TDESMD with an infinitely long Rabi period and zero frequency. The simplified MD and ESMD calculations are needed for identifying all pathways, including inefficient pathways. On short time intervals, the TDESMD trajectory may evolve similarly to MD or ESMD trajectories, used as a reference data. By comparing TDESMD to simpler methods we highlight the role of electronic transitions.

The procedure of TDESMD was described in detail in previous work.[37] Briefly, in TDESMD simulation, the photofragmentation process is explored by periodic excitations and de-excitations of the model due to the light-matter interaction term in total energy and in the Fock matrix $\hat{F}$ as follows,

$$\hat{F} = \hat{F}^{KS} + \hat{V}^{NA}(t) - \widehat{\vec{M}} \cdot \vec{\varepsilon}(t) \tag{1}$$

where $\hat{F}^{KS}$ stands for ground state Fock matrix, $\hat{V}^{NA}(t)$ represents nonadiabatic couplings, $\widehat{\vec{M}}$ stands for transition dipole operator, $\vec{\varepsilon}(t) = \vec{\varepsilon} \cdot \cos(\Omega t)$ is the electric field of laser, and $\Omega$ is the laser field frequency.[44,45] In presence of the laser field of high intensity, the electrons experience transitions $i \rightarrow j$ and $i \leftarrow j$ between ground state, $i$, and excited state, $j$, with the transition-specific Rabi frequency, $\hbar\Omega_{ij}^R$,

$$\hbar\Omega_{ij}^R = \langle i|\widehat{\vec{M}}|j\rangle \cdot \vec{\varepsilon} \tag{2a}$$

$\vec{M}_{ij}$ is the electric dipole moment matrix element for the transition between the initial state $i$ and the final $j$ state. $\vec{M}_{ij}$ is expressed as

$$\langle i|\vec{M}|j\rangle = \vec{M}_{ij} = e \int \varphi_i^* \vec{r} \varphi_j \, d\vec{r} \tag{2b}$$

It uses the summation of the position of all electrons in the system ($\vec{r}$) and elementary charge ($e$). Although the methodology is generally applicable to multi-electron excitations here we approximate an excitation by a pair of non-interacting orbitals, occupied, $i$ and unoccupied, $j$. Thus an excited state is labeled by a pair of orbital indices $(i,j)$. $\vec{M}_{ij}$ is also used to compute absorption spectra as outlined in Supporting Information, eqs S1 and S2. Calculation of absorption in the approximation of noninteracting orbitals is a standard tool for large models where more precise treatment is not available.[46−49] This approach is especially useful for quantum dots.[50] At each instant of time, the system is characterized by the positions of nuclei $\{\vec{R}_I(t)\}$ for the nuclear system, and by the electronic densities/density matrix for the electronic system. Both electronic and nuclear degrees of freedom evolve in time in a coupled way. The nonadiabatic couplings can provide an additional channel for transitions between electronic states. Nonadiabatic couplings between electronic and nuclear degrees of freedom originate from a matrix element of kinetic energy of nuclei on the basis of electronic wave functions as and consists of two terms including first (I) and second (II) derivatives with respect to nuclear position displacement $\vartheta_{ij} = \omega_{ij}^{(I)} + \omega_{ij}^{(II)}$. Here $\omega_{ij}^{(I)} = \Sigma_I (i\hbar/2M_I) \langle \phi_i |(\partial/\partial\vec{R}_I)|\phi_j\rangle \vec{P}_I$ and $\omega_{ij}^{(II)} = \Sigma_I (-\hbar^2/2M_I) \langle \phi_i |(\partial^2/\partial\vec{R}_I^2)|\phi_j\rangle$. Typically, one assumes $\omega_{ij}^{(I)} \gg \omega_{ij}^{(II)}$ and keeps only linear term $\vartheta_{ij} \approx \omega_{ij}^{(I)}$. Numerical values of the nonadiabatic couplings can be found in two equivalent ways: (i) based on the derivative of Hamiltonian (Fock operator), in the basis of KS orbitals |i> and |j> with respect to the position of $I$th nuclei $\vec{R}_I$ or (ii) according to the on-the-fly procedure, in finite differences $\vartheta_{ij} = V_{ij}^{NA}(t) = -i\hbar < \varphi_i^{KS}(\vec{r},\{\vec{R}_I(t)\})|(d/dt)|\varphi_j^{KS}(\vec{r},\{\vec{R}_I(t)\})>$. Nonadiabatic couplings are efficiently computed according to an on-the-fly procedure.[24,51,52] However, for this problem $|V^{NA}| < |\vec{M} \cdot \vec{\epsilon}|$ as discussed below. The electronic degrees of freedom obey the equation of motion for the density operator $\hat{\rho}$, which is often cast in terms of the Liouville−von Neumann superoperator $\mathcal{L}$ and Redfield superoperator $\mathcal{R}$.

$$\frac{d}{dt}\hat{\rho} = -\frac{i}{\hbar}[\hat{F}, \hat{\rho}] + \left(\frac{d\rho_{ij}}{dt}\right)_{diss} = (\mathcal{L} + \mathcal{R})\hat{\rho} \tag{3a}$$

Here, $(d\rho_{ij}/dt)_{diss} = \sum_{lm} R_{jklm}\rho_{lm}$ are electronic dissipative transitions, which are facilitated by an average motion of ions computed along molecular dynamics trajectory. Elements of Redfield tensor, $R_{jklm}$, control dissipative dynamics of density matrix. For practical calculations, the density operator must be represented in a specific basis.[53,54] Here we choose the basis of KS orbitals with one-particle density matrix $\rho_{ij}(t)$ playing the role of expansion coefficients as defined in what follows.

$$\rho(\vec{r}, t) = \sum_{ij} \rho_{ij}(t) \cdot \varphi_i^{KS}(\vec{r}, \{\vec{R}_I(t)\}) \cdot \varphi_j^{KS}(\vec{r}, \{\vec{R}_I(t)\}) \tag{3b}$$

Prior to dynamics, density at initial time determining the relative contribution of KS orbitals is weighted by one-electron density matrix $\rho_{ij}(t = 0)$ satisfying the following initial conditions,

$$\rho_{ij}(t = 0) = \rho_{ij}^{eq}; \quad \rho_{ij}^{eq} = \delta_{ij}f_i; \quad f_i = \begin{cases} 0, & i \geq LU \\ 1, & i \leq HO \end{cases} \tag{3c}$$

The orbitals $\phi_i^{KS}(\vec{r},\{\vec{R}_I(t)\})$ and orbital energies $\varepsilon_i(\{\vec{R}_I(t)\})$ can be obtained from the model at optimized geometry, at initial time $t = 0$, and from updated geometry at later times and used to calculate the electronic dynamics for the subsequent increment of time, $\Delta t$. At each step, the updated density is obtained with known increment: $\rho_{ij}(t + \Delta t) = \rho_{ij}(t) + \Delta\rho_{ij}$. Here $\Delta\rho_{ij}$ is a finite time increment, which accounts for the transitions between electronic degrees of freedom. Then through the new density matrix $\rho_{ij}(t + \Delta t)$, one updates three key variables characterizing the model: (i) new total charge density, (ii) the new orbitals and their energies, and (iii) new interatomic forces and positions of ions. The density matrix can also be explicitly propagated in time by diagonalizing the Liouville−von Neumann and Redfield superoperator $\mathcal{L} + \mathcal{R}$ at each time step.[55−60] Here, propagation of electronic degrees of freedom is modeled via instantaneous surface hopping between potential energy surfaces, as an approximation.[22] Occupation of orbitals experiences a change in time, with the major contribution provided by oscillating with Rabi frequency $\Omega_{ij}^R$. A stepwise change in occupations of two interacting orbitals $i$ and $j$ is introduced as follows,

$$\rho_{ii} = 1 \xrightarrow{\Delta t} \rho_{ii} = 0, \quad \Delta\rho_{ii} = -1 \tag{3d}$$

$$\rho_{jj} = 0 \xrightarrow{\Delta t} \rho_{jj} = 1, \quad \Delta\rho_{jj} = +1 \tag{3e}$$

Such stepwise changes are implemented in replacement of continuous oscillations. This approximation to Rabi theory helps to avoid the mean-field paradox. Instantaneous hopping between potential energy surfaces was introduced by Tully,[22−24,61] as a surface-hopping method, which is a reliable way for predicting interatomic forces.[62] The Fock matrix is updated at each time step, following changes in forces, geometry, and density. The Fock potential is updated when the nuclei moved. A change of the electronic configuration and change of the potential energy surface determine a change in the interatomic forces. Thus, nuclear configuration represented by the position of nuclei $\{\vec{R}_I(t)\}$ and the electronic configuration represented by density matrix $\rho_{ij}(t)$, evolve in time in a coupled and consistent way. As a result, the time dependent density matrix, $\rho_{ij}(t)$, experiences a rapid change in time due to light perturbation for excitations that match the laser frequency $(\varepsilon_i - \varepsilon_i) \approx \hbar\Omega_{ij}$. Note that $\Omega_{ij}^R \neq \Omega_{ij}$. The total density, recomputed according to eq 3b is then used in the Kohn−Sham self-consistent procedure, and determines the energy gradient and forces imposed on each nuclei of the model,

$$\frac{d^2}{dt^2}\vec{R}_I(t) = \vec{F}_I(t)/M_I \tag{3f}$$

Light-induced changes in the electronic configuration and forces $\vec{F}_I([\vec{\rho}(t)])$, which depend on the phase of incident light, allow the nuclear positions to overcome the dissociation barriers and result in a rich fragmentation dynamics trajectory. An optically driven change of electronic state has a smaller random component than trajectories driven by electron-to-nuclei interactions, since the intensity of electronic transitions driven by photons is higher than that driven by nuclear motion.

All trajectories in the swirl would be the same. Therefore, we propagate only one trajectory, where electronic transitions are induced by the laser field.

Each of three introduced methods of molecular dynamics allows computation of a nuclear *trajectory* for given initial conditions. A trajectory includes several hundred time steps with different nuclear configurations at each step representing intermediates and products of the photofragmentation reaction. At each step the nuclear configuration is evaluated for a number of fragments.[33] The interatomic bond distance for each pair of nuclei is used to evaluate whether a chemical bond is breaking or forming, and thus to determine the number of fragments, $f_{max}$, number of nuclei in each fragment, $I^{(f)}_{max}$, and the composition of each fragment, with all above being time dependent. Thus, a single list of nuclei in the model is replaced by a separate list of nuclei for each fragment.

$$\{\vec{R}_I(t)\}_{I=1...I_{max}} \rightarrow \begin{cases} \underbrace{\{\vec{R}_{I^{(1)}}(t)\}^{f=1}_{I^{(1)}=1...I^{(1)}_{max}}}_{\text{first fragment}}, \\[2mm] \underbrace{\{\vec{R}_{I^{(2)}}(t)\}^{f=2}_{I^{(2)}=1...I^{(2)}_{max}}, \quad ...,}_{\text{second fragment}} \\[2mm] \underbrace{\{\vec{R}_{I^{(f_{max})}}(t)\}^{f=f_{max}}_{I^{(f_{max})}=1...I^{(f_{max})}_{max}}}_{\text{last fragment}} \end{cases}$$

(4)

Here, $f$ is the index for a fragment, such that $1 \leq f \leq f_{max}$. $I^{(f)}_{max}(t)$ is the number of nuclei in a fragment number $f$, and $I^{(f)}$ is an index labeling nuclei in a fragment number $f$, such that $1 \leq I^{(f)} \leq I^{(f)}_{max}$. $\vec{R}_{I^{(f)}}$ is the position of nucleus number $I^{(f)}$ from the fragment number $f$. Note that the composition and size of each fragment reconfigure with time.

**2.3. Simulated Mass Spectra.** The fragmentation of the model system can be summarized in the form of simulated mass spectra. Simulated mass spectra can be extracted from TDESMD, ESMD, and MD trajectories. Our goal is to simulate PI−TOF mass spectra by predicting possible products of photofragmentation and compare with experimental PI−TOF mass spectra. Such comparison is reasonable in the mass range between $La^+$ and $La(iCp)^+$. In the experimental PI−TOF mass spectra, all features are assigned with +1 charge in the mass range between $La^+$ and $La(iCp)^+$, so that the mass-to-charge ratio of any fragment equals the mass of this fragment. $M_f(t)$ is the molecular mass of fragment $f$ and can be calculated according to,

$$M_f(t) = \sum_{I^{(f)}=1}^{I^{(f)}_{max}(t)} M_{I^{(f)}}(t)$$

(5a)

where $M_{I^{(f)}}$ is the mass of ion number $I^{(f)}$ belonging to fragment $f$. The mass spectrum, $MS(m_z, t)$, at instantaneous time, $t$, is expressed as,

$$MS(m_z, t) = \sum_{f=1}^{N_f(t)} \delta(M_f(t) - m_z)$$

(5b)

where $N_f(t)$ is number of fragments, and $f$ is an index labeling fragments $1 \leq f \leq N_f$. $M_f(t)$ is the mass of a given fragment, $f$. $m_z$ is an argument, which scans all possible values of molecular weight. The Dirac delta function, $\delta(M_f(t) - m_z)$, is approximated by a finite-width Lorentzian function:

$$\delta(x) = \frac{1}{\pi} \frac{\sigma}{\sigma^2 + x^2}$$

(6)

where $\sigma$ is a parameter with the same dimensions as the argument of the Delta function which gives the width of the distribution. The value $\sigma = 0.1$ was used to simulate spectral line broadening in experimental mass spectra. The simulated mass spectra, $\langle MS \rangle(m_z)$, are calculated by performing an average along the duration of the trajectory in eq 5:

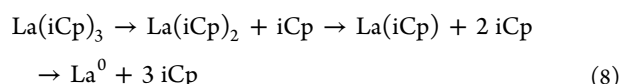$$\left\langle MS \right\rangle(m_z) = \frac{1}{T} \int_0^T MS(m_z, t) \, dt$$

(7)

Equations 5 and 7 perform the conversion of the AIMD trajectory $\{\vec{R}_I(t)\}$ into mass spectra $\langle MS \rangle(m_z)$ with several limitations and approximations:

(1) In this method, the simulated mass spectra were computed from one single trajectory. We expect a better result would be reached by extracting the mass spectra from an ensemble of multiple trajectories and then weighted according to the oscillator strength of initial excitation for each trajectory.

(2) Optical excitation is modeled in an elementary way, involving a single electron−hole pair.

(3) Currently, a "frozen step" approach is used to analyze each stage of the trajectory, as shown in eq 4. A snapshot of a trajectory at a given time is converted into fragments by neglecting momentum and kinetic energy, in a similar way as it would be done for equilibrated geometry. Such an approach may lead to ambiguity in identifying a bond as being intact or broken in the vicinity of the bond-breaking regime, $R_0 < R < R_B$. Specifically, any interatomic distance to the left of a barrier in Figure 1 is intact if the energy $U(R) < U(R_B)$.

(4) Our current approach to process the TDESMD trajectory is new and differs from earlier publications.[37,38]

Differences in post processing methods could be responsible for some differences in how trajectories are interpreted.

## 3. RESULTS

Previous PI−TOF experimental studies[12−15,37,38] have shown that the species involved in the dominant photoreactions are neutral and are detected by the mass spectrometry following postdissociation photoionization. In this study we model the first step of the photofragmentation process. The second step of the post-dissociation photoionization process is simply the experimental sampling method and is not explicitly modeled. Because simulations starting from $La(iCp)_3$ would require excessive computational resources, the neutral initial model used was $La(iCp)$, built with a single iCp ring $\eta^5$ bonded to a central lanthanum ion. $La(iCp)$ is one of the important intermediates generated in the fragmentation of $La(iCp)_3$. This intermediate is expected to be less stable than the initial precursor. In the PI−TOF mass spectra of $La(iCp)_3$, the peak at $m/z = 246$ corresponding to $La(iCp)^+$ is observed, even though the intensity is weak. $La(iCp)$ is thought to be produced through a reaction pathway of

$$\text{La(iCp)}_3 \rightarrow \text{La(iCp)}_2 + \text{iCp} \rightarrow \text{La(iCp)} + 2\,\text{iCp}$$
$$\rightarrow \text{La}^0 + 3\,\text{iCp} \tag{8}$$

with each step mediated by excitation to the ligand-to-metal charge-transfer state similar to the mechanism proposed for several lanthanide complexes.[12−15,37,38] The neutral La(iCp) fragment could lead to the formation of other neutral species with smaller $m/z$. La(iCp) was selected as the theoretical starting atomic model due to the balance of needs and computational abilities. The simulation cell consists of the La(iCp) atomic model with a 7 Å vacuum in each direction, $x$, $y$, $z$, to minimize interactions between fragments and penetrations from adjacent simulation cells. In the simulation we keep total charge of the simulation cell fixed at zero. Local rearrangements of charge density and charge transfer events are possible inside one fragment and between different fragments inside the simulation cell during the simulation. Additional calculations for fragmentation of ionized species i.e. La(iCp)$^{2+}$ have also been explored and are presented in the Supporting Information.

The density of states (DOS) and projected density of states (PDOS) for unperturbed La(iCp) computed by ground state DFT and the partial charge density isosurfaces for selected Kohn−Sham orbitals visualized by VMD[63] software are shown in Figure 2. In the DOS, features $a$ (HO−2), $b$ (HO−1), and $h$ (LU+12) show that the charge density is concentrated on the carbons of the iCp ligand. Features $c$ (HO), $d$ (LU), $e$ (LU+3), $f$ (LU+10), and $g$ (LU+11) show the dominant portion of the charge density is located on La ion. Specifically, for feature $a$ and $b$, the contribution is mainly from the p orbitals of carbon, but there are also minor contributions from the d orbital of La. Feature $c$ shows orbitals of s, p, d, and f character from La, with the largest contribution from the d orbitals. Features $d$ and $e$ show all seven orbitals of f character, with the largest contributions from contributions from orbitals with magnetic quantum number values $m_z = -1$ and $m_z = 0$, respectively. Features $f$ and $g$ show orbitals with p, d, and f from La, with the largest contribution from d orbitals. There are some minor contributions from the p orbitals of carbon. Feature $h$ shows the orbitals with s and p character delocalized over carbons and La.

The calculated absorption spectrum of the unperturbed La(iCp) model is shown in Figure 3. The most intense peaks are found at ~0.3 eV and ~1.2 eV. The transitions corresponding to these peaks are from HO to unoccupied orbitals, with contributions from the d−f and d−d transitions on La, respectively. In this study, these transitions were not explored in TDESMD simulations, because it was found that laser-driven photoreactions were initiated by the ligand-to-metal charge-transfer (LMCT) process at higher energies.[38]

As shown in Figure 3, the transition energy of HO−2 → LU+3 and HO−2→ LU+11 is about 3.59 eV ($\lambda \approx 345$ nm) and 4.70 eV ($\lambda \approx 264$ nm), respectively. These transitions have relatively large oscillator strengths, and are typical LMCT transitions, as illustrated in Figure 2. They are more likely to facilitate the photofragmentation of the model. In TDESMD calculations, the transitions labeled in Figure 3 are chosen to simulate the laser perturbation of the model.

In TDESMD simulations, the inverse Rabi frequency, $2\pi\Omega_R^{-1} = 10$ fs. Time increments for simulations are 1 fs. The duration of the simulations is 800 fs. At each time step, we are only focusing on La-containing fragments in the mass range
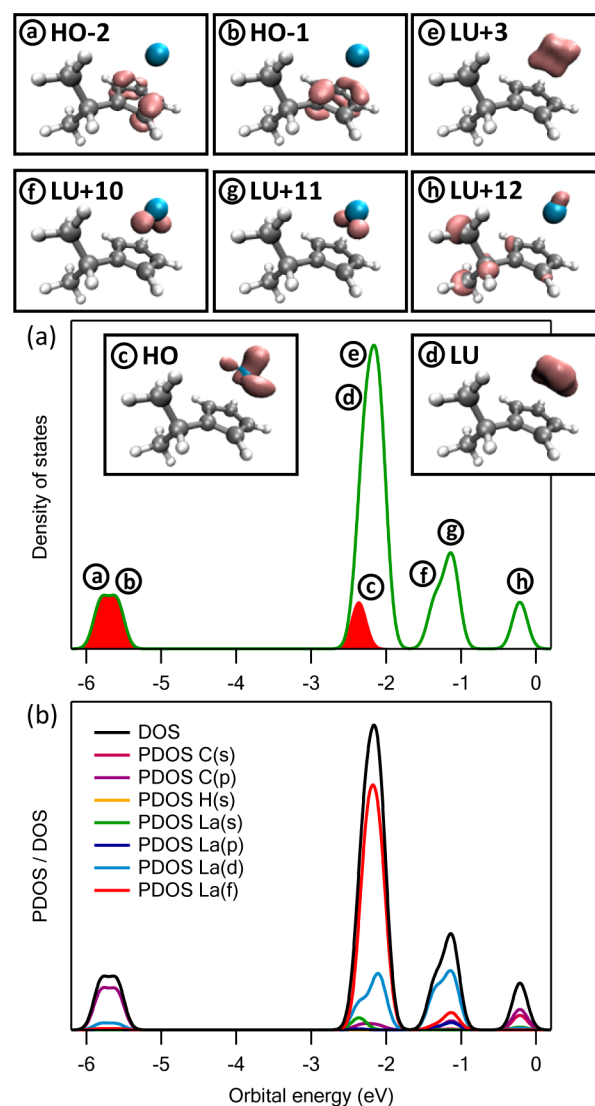


**Figure 2.** (a) Density of states for unperturbed La(iCp) computed by ground state DFT and partial charge density for selected Kohn−Sham orbitals. The filled area corresponds to occupied orbitals and the unfilled area corresponds to unoccupied orbitals. Positions in the DOS indicate intervals of energy containing certain orbitals. Each orbital is labeled based on HOMO−LUMO notation and illustrated by isosurfaces of partial charge density. LU+$n$ means the $n$th orbital above LU and HO−$n$ means the $n$th orbital below HO. The blue, gray, and white spheres represent La, C, and H, respectively. Isosurfaces are in pink. (b) Partial density of states and density of states for unperturbed La(iCp) computed by ground state DFT. Isosurfaces of partial charge density are created by using VMD software.[63]

between La$^+$ ($m/z = 139$) and La(iCp)$^+$ ($m/z = 246$). Dynamics of formation of species with smaller $m/z$ ($m/z < 139$) is not considered. One reason for this is that, in the low mass region, the experimental PI−TOF mass spectra show features (fragments containing no La ion) with relatively low intensity and are likely to be influenced by contaminants. Therefore, it would be difficult to evaluate the simulation results relative to experimental data.

Table 1 shows representative snapshots of fragments occurring during the TDESMD simulation with electrons hopping between the ground state, HO−2, and the excited state, LU+3, corresponding to wavelength $\lambda \approx 345$ nm used to compute simulated mass spectra. The snapshots are created by
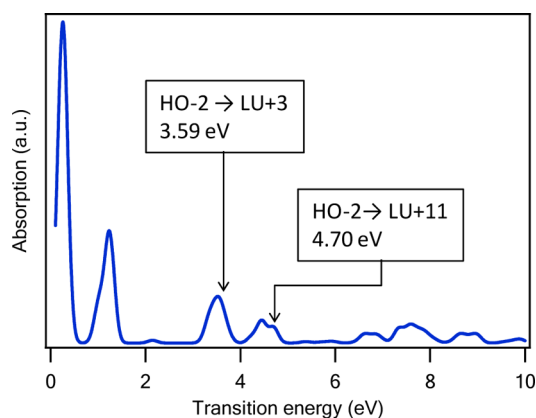
**Figure 3.** Absorption spectrum for unperturbed La(iCp) computed by ground state DFT in the approximation of independent orbitals, using equations 2b, S1, and S2. The transition energy of HO−2 → LU+3 and HO−2→ LU+11 is about 3.59 eV, corresponding to wavelength $\lambda \approx 345$ nm, and 4.70 eV, corresponding to wavelength $\lambda \approx 264$ nm, respectively. These transitions are typical ligand-to-metal charge-transfer transitions and are explored in the TDESMD simulation.

using Jmol.[64] Hydrocarbon fragments desorbed away from the central fragment are not shown for clarity, except for the b and c fragments. It should be noted that the geometry of each shown fragment might be different from the equilibrium configuration, since all ions participate in dynamics, and have nonzero momentum.

Figure 4 shows the time evolution of simulated mass spectra generated from TDESMD simulations using transitions between the ground state, and the excited state, characterized by the pair of orbitals (HO−2; LU+3) corresponding to wavelength $\lambda \approx 345$ nm. Only a few fragments, such as La, LaH, and La(iCp), are observed in the first 400 fs. These fragments
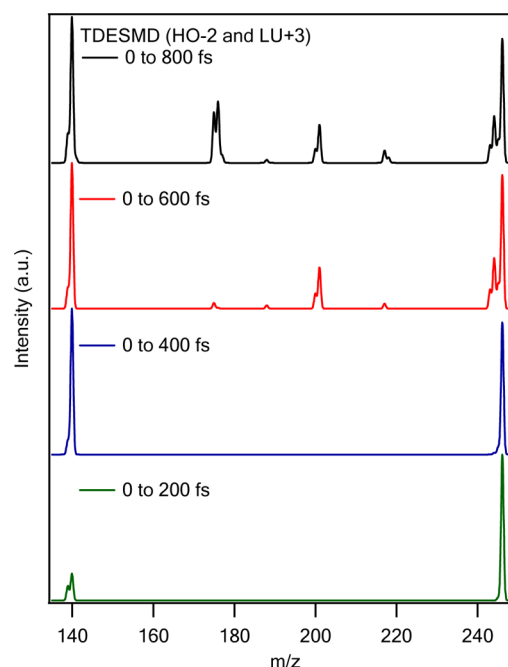


**Figure 4.** Time evolution of mass spectra derived from TDESMD simulations using transitions between the ground and excited state characterized by pair of orbitals (HO−2; LU+3), corresponding to wavelength $\lambda \approx 345$ nm in an inverse Rabi frequency $2\pi\Omega_R^{-1} = 10$ fs from 0 to 800 fs (black), 600 fs (red), 400 fs (blue), and 200 fs (green).

could be artifacts of the "frozen step" approximation. Fragments become abundant after 400 fs, because of noticeable energy accumulation.

**Table 1. Representative Snapshots of Fragments Containing La Used To Compute Simulated Mass Spectra during TDESMD Simulation with Transitions Between the Ground State and the Excited State, Characterized by the Pair of Orbitals (HO−2; LU+3), in an Inverse Rabi Frequency $2\pi\Omega_R^{-1} = 10$ fs**



| (a) 0 fs, $LaC_8H_{11}$ | (b) 169 fs, La | (c) 174 fs, LaH | (d) 421 fs, $LaC_8H_{10}$ |
| (e) 422 fs, $LaC_8H_9$ | (f) 509 fs, $LaC_8H_8$ | (g) 517 fs, $LaC_5H_2$ | (h) 526 fs, $LaC_5H$ |
| (i) 565 fs, $LaC_4H$ | (j) 589 fs, $LaC_3$ | (k) 596 fs, $LaC_6H_6$ | (l) 617 fs, $LaC_6H_7$ |
| (m) 670 fs, $LaC_3H$ | (n) 787 fs, $LaC_3H_2$ | (o) 794 fs, $LaH_2$ | |

Figure 5 shows a comparison between the PI−TOF mass spectrum of La(iCp)$_3$ with photoexcitation at $\lambda$ = 266 nm and



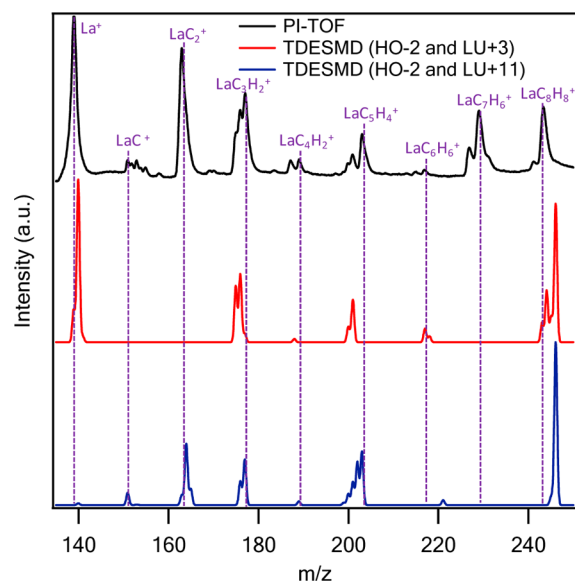**Figure 5.** PI−TOF mass spectrum of La(iCp)$_3$ with photoexcitation at 266 nm (black) and simulated mass spectrum from TDESMD simulations with transitions between the ground state and the excited state, characterized by the pair of orbitals (HO−2; LU+3) (red) corresponding to wavelength $\lambda \approx$ 345 nm and between the ground state and the excited state, characterized by the pair of orbitals (HO−2; LU+11), (blue) corresponding to wavelength $\lambda \approx$ 264 nm in an inverse Rabi frequency $2\pi\Omega_R^{-1}$ = 10 fs. Vertical dashes indicate the most intense peak in each group of fragments in terms of number of carbons observed in experimental PI−TOF mass spectrum.

the simulated mass spectra from TDESMD using La(iCp) as the starting point. Simulated spectra are generated for two different excitation energies. $\lambda \approx$ 345 nm corresponds to transition between the ground state and the excited state, characterized by the pair of orbitals (HO−2; LU+11) (blue spectrum). It is found that each of the simulated mass spectra reproduce some of features observed in the experimental PI−TOF mass spectra, even though the relative intensity differs. In addition, it is found that TDESMD simulations from the different trajectories generate different fragments, indicating that the fragmentation pathway depends on the excitation energy. It should be noted that there are still some observed features that are not reproduced in either of the TDESMD simulations. For example, LaC$_7$H$_n$ ($n$ = 4−8) peaks are observed in the PI−TOF mass spectra, but not in the mass spectra of TDESMD simulations. A possible reason is explored in the Discussion.

Figure 6 shows the PI−TOF mass spectrum of La(iCp)$_3$ produced with photoexcitation at $\lambda$ = 266 nm compared to simulated mass spectra from TDESMD, ESMD, and MD simulations using La(iCp) as the starting point. This comparison is performed in order to test if the fragmentation pathway depends on the excitation mechanism. In TDESMD, transitions occur between the ground state, and the excited state, characterized by the pair of orbitals (HO−2; LU+3), corresponding to wavelength $\lambda \approx$ 345 nm. In ESMD, electrons are promoted from the ground state, to the excited state, characterized by the pair of orbitals (HO−2; LU+3) where they remain during the dynamics. In MD, the system resides in the
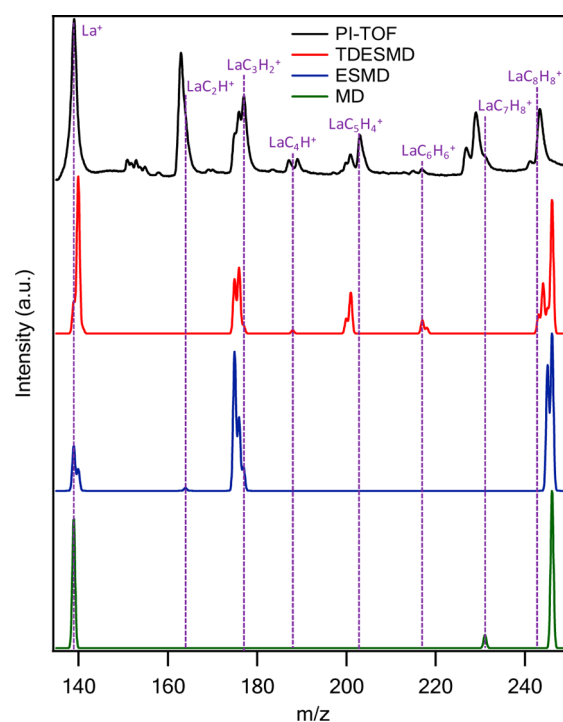


**Figure 6.** PI−TOF mass spectrum of La(iCp)$_3$ with photoexcitation at 266 nm (black) and simulated mass spectrum from TDESMD (red), and ESMD (blue), and MD (green) using La(iCp) as the starting point in the mass range between La$^+$ and La(iCp)$^+$. In TDESMD the transitions occur between the ground state, and the excited state, characterized by the pair of orbitals (HO−2; LU+3), with an inverse Rabi frequency $2\pi\Omega_R^{-1}$ = 10 fs. In ESMD the model is promoted from the ground state to the excited state, characterized by the pair of orbitals (HO−2; LU+3). In MD electrons are in ground state and run at the temperature that mimics the TDESMD trajectory. Each method produces a different distribution of products. Vertical dashes indicate the most intense peak in each group of fragments in terms of number of carbons from experimental PI−TOF mass spectrum reproduced by simulated mass spectra.

ground electronic state and experiences a linearly increasing temperature in a regime that mimics the amount of kinetic energy of ions accumulated by the model in the TDESMD simulation trajectory. To facilitate comparison, the time increments and duration of simulations in ESMD and MD are the same as those in TDESMD.

Figure 6 shows clearly that the TDESMD simulation exhibits the greatest similarity with experimental PI−TOF mass spectrum. The largest discrepancy is found for the MD simulated spectrum. The fragments observed in experimental PI−TOF and generated in the simulated mass spectra are listed in Table 2 and Table S1. In Table 2, we note the ability of a method to reproduce groups of fragments with given number of carbons, LaC$_m$H$_n$, m = 0−8. The experimental PI−TOF mass spectrum exhibits 9 groups. The TDESMD, ESMD, and MD simulations exhibit 6, 4, and 3 groups, respectively. A description of each fragment in the various simulated mass spectra as well as a comparison of features between experimental and simulated mass spectra can be found in Table S1. A comparison of the mass spectra from the different simulation methods indicates that the fragmentation depends on the manner in which excitation energy has been communicated to the molecule.

**Table 2. Summary of Fragments in Experimental PI−TOF Mass Spectrum and Simulated Mass Spectra from TDESMD, ESMD, and MD Simulations**

| no. of carbons | m/z | Fragment observed in PI−TOF | appearance of at least one fragment from a given group in simulated mass spectra of a given method | | |
|---|---|---|---|---|---|
| | | | TDESMD[a] | ESMD[b] | MD[c] |
| 8 | 241, 243−246 | $LaC_8H_n$ (n = 6, 8−11) | Y | Y | Y |
| 7 | 227−231 | $LaC_7H_n$ (n = 4−8) | N | N | Y |
| 6 | 213, 215−217 | $LaC_6H_n$ (n = 2, 4−6) | Y | N | N |
| 5 | 199−204 | $LaC_5H_n$ (n = 0−5) | Y | N | N |
| 4 | 187−191 | $LaC_4H_n$ (n = 0−4) | Y | N | N |
| 3 | 175−178 | $LaC_3H_n$ (n = 0−3) | Y | Y | N |
| 2 | 163−165 | $LaC_2H_n$ (n = 0−2) | N | Y | N |
| 1 | 151−155 | $LaCH_n$ (n = 0−4) | N | N | N |
| 0 | 139 | La | Y | Y | Y |
| total | | | 9 | 9 | 9 |
| coincidence | | | 6 | 4 | 3 |
| miss | | | 3 | 5 | 6 |

[a]Model experiences periodic transitions between the ground state, and the excited state, characterized by the pair of orbitals (HO−2; LU+3) with an inverse Rabi frequency $2\pi\Omega_R^{-1} = 10$ fs. [b]Model is promoted from the ground state, to the excited state, characterized by the pair of orbitals (HO−2; LU+3). [c]Electrons are in the ground state.

During the simulation process, the model accumulates kinetic energy. A gradient of total energy in respect to nuclei's positions induces motion toward potential energy surface minima, which lowers potential energy and increases kinetic energy. With increasing simulation time, the eventual excess in kinetic energy overcomes the dissociation barriers for several subsequent reactions and leads to fragmentation. Figure 7 shows the total energy as a function of time during the TDESMD, ESMD, and MD simulations.

The total energy profile for three types of simulations is observed as $E_{tot}^{MD}(t) \lesssim E_{tot}^{TDESMD}(t) \lesssim E_{tot}^{ESMD}(t)$. The total energy, in all cases, increases linearly with time, according to

$$E_{tot}(t) = E_{tot}(0) + xt + \delta E(t) \qquad (9)$$

where $x$ is the energy accumulation rate. The values of $x$ for the various models are $x^{TDESMD} \approx 0.035$ eV/fs, $x^{ESMD} \approx 0.045$ eV/fs, and $x^{MD} \approx 0.052$ eV/fs. $\delta E(t)$ represents random energy fluctuations at each instant in time. It is found that energy portion of about 32.4, 39.8, and 39.2 eV are accumulated during the TDESMD, ESMD, and MD simulations, respectively. It is interesting that the TDESMD simulation generates the most fragments, as illustrated in Table 2 and Table S1, but accumulates the least energy during the simulation. This result emphasizes that the amount of energy added to the system plays secondary role in determining the photofragmentation pattern.

## 4. DISCUSSION

The challenging goal of modeling and predicting laser driven reaction dynamics was partially met with chosen approximations. However, several details of the modeling are not yet resolved. Here, we provide an outlook for open issues and possible ways to address them. A detailed analysis of nonadiabatic couplings and their change in time is provided in Supporting Information. It is interesting and important that the average transition rate between any pair of orbitals never exceeds 0.05 fs$^{-1}$ corresponding to the relaxation time of 20 fs. It indicates that the quickest pathway of the radiative transitions is slower than the adopted Rabi frequency in the TDESMD simulations. Therefore, we assume that Rabi oscillations induced by optical transitions play a dominant role in determining chemical reactions of photofragmentation.

The simulated mass spectra of TDESMD from a single trajectory cannot reproduce all features of the PI−TOF mass spectra, as the latter show fragments from many trajectories. Therefore, to reproduce all observed fragments in the PI−TOF mass spectra, simulated TDESMD mass spectra should be obtained from different trajectories. One strategy is to use different excitation energies by selecting different occupied and unoccupied orbital pairs for TDESMD calculations.

Some experimentally observed fragments are not reproduced by the simulated mass spectra from the selected TDESMD trajectories presented in this paper. We expect that some of the
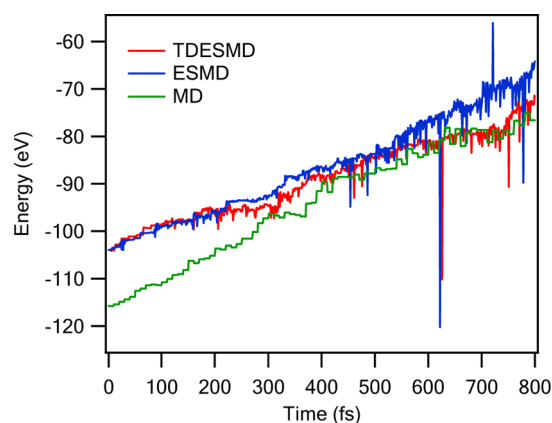
**Figure 7.** Total energy as a function of simulation time for TDESMD (red), ESMD (blue), and MD (green). In TDESMD, the model experiences periodic transitions between the ground state, and the excited state, characterized by the pair of orbitals (HO−2; LU+3) with an inverse Rabi frequency $2\pi\Omega_R^{-1} = 10$ fs. In ESMD, the electronic state of the model is promoted from the ground state to the excited state, characterized by the pair of orbitals (HO−2; LU+3). In MD, electrons remain in ground state and run at the temperature that mimics the TDESMD trajectory. The rate of energy accumulation for each method is $x^{TDESMD} \approx 0.035$ eV/fs, $x^{ESMD} \approx 0.045$ eV/fs, and $x^{MD} = 0.052$ eV/fs. TDESMD and ESMD have a higher initial energy than MD, because TDESMD and ESMD simulations begin with electrons in the excited state at time zero, whereas MD begins with electrons in the ground state.

missing fragments could be reproduced by TDESMD simulated trajectories corresponding to different excitation energies. Other fragments may require a different starting point, e.g. La(iCp)$_2$, in the fragmentation. Such studies will be pursued in the future.

It should be noted that simulated mass spectra computed by each of the methods considered here, TDESMD, ESMD, and MD, may produce additional features which are not observed in the experimental mass spectra. For instance, the mass spectrum from the TDESMD simulation with electron's hopping between the ground state, HO−2, and the excited state, LU+3, shows the presence of LaH$_2$. The simulation based on electron's hopping between the ground state, HO−2, and the excited state, LU+11, shows the feature LaC$_6$H$_{10}$. The additional features seen in the simulated mass spectra may be due to the limits in the way the simulation methods are implemented. In the reported simulations, the dissociated fragments are kept inside the simulation cell all the time instead of being allowed to drift away from the system. Therefore, the dissociated fragments are likely to be recaptured or undergo further decomposition and recombine with other fragments to give additional features. Since the simulation cell contains several fragments moving with nonzero velocity, the modeling environment can be interpreted as a gas phase rather than a vacuum.

The inconsistent intensity pattern between simulated mass spectra and the experimental PI−TOF mass spectra should not be surprising because the calculations use a model compound La(iCp) instead of the larger species La(iCp)$_3$. La(iCp) is thought to be created in the PI−TOF experiment and a source of additional fragmentation, but the experimental measurement would also include fragments originating from La(iCp)$_2$ and La(iCp)$_3$, lacking in the simulation. In addition, the measurement involves multiple channel (dissociation/ionization) and multiphoton processes that are not considered by the computational modeling.

## 5. CONCLUSIONS

In this study, the photofragmentation of La(iCp) was explored through TDESMD, ESMD, and MD simulations. In addition, we reported a simple method to simulate mass spectra from TDESMD, ESMD, and MD simulations. Among the three simulation methods, TDESMD produced the best comparison with the experimental spectrum. However, because considerable inconsistency exists between the measured and TDESMD predicted intensity patterns, further work is needed to improve the computational model and used approximations. The simulated mass spectra from different TDESMD trajectories generate different products, indicating the dissociation process depends on the excitation energy. A comparison of simulated mass spectra of TDESMD, ESMD, and MD indicates the manner of excitation also determines the dissociation pathway. We hope our method of extracting mass spectra could not only be used in obtaining mass spectra of photoreactions but also shed light or provide insights to a broader range of reactions such as explosion.

## ASSOCIATED CONTENT

### Ⓢ Supporting Information

The Supporting Information is available free of charge on the ACS Publications website at DOI: 10.1021/acs.jpca.5b07209.

Calculation of absorption spectra, approximations for TDESMD simulations, summary of fragments and nonadiabatic coupling for neutral La(iCp), electronic structure, absorption, and simulated mass spectra from La(iCp)$^{2+}$ (PDF)

## AUTHOR INFORMATION

### Corresponding Author

*(D.S.K.) E-mail: Dmitri.Kilin@usd.edu; Dmitri.Kilin@ndsu.edu.

### Notes

The authors declare no competing financial interest.

## REFERENCES

(1) Schlom, D. G.; Haeni, J. H. A Thermodynamic Approach to Selecting Alternative Gate Dielectrics. *MRS Bull.* **2002**, *27*, 198−204.

(2) Hong, M.; Kwo, J.; Kortan, A. R.; Mannaerts, J. P.; Sergent, A. M. Epitaxial Cubic Gadolinium Oxide as a Dielectric for Gallium Arsenide Passivation. *Science* **1999**, *283*, 1897−1900.

(3) Osten, H. J.; Laha, A.; Czernohorsky, M.; Bugiel, E.; Dargis, R.; Fissel, A. Introducing Crystalline Rare-Earth Oxides into Si Technologies. *Phys. Status Solidi A* **2008**, *205*, 695−707.

(4) Bonnet, G.; Lachkar, M.; Colson, J. C.; Larpin, J. P. Characterization of Thin Solid Films of Rare Earth Oxides Formed by the Metallo-Organic Chemical Vapour Deposition Technique, for High Temperature Corrosion Applications. *Thin Solid Films* **1995**, *261*, 31−36.

(5) Kanarjov, P.; Reedo, V.; Oja Acik, I.; Matisen, L.; Vorobjov, A.; Kiisk, V.; Krunks, M.; Sildos, I. Luminescent Materials Based on Thin Metal Oxide Films Doped with Rare Earth Ions. *Phys. Solid State* **2008**, *50*, 1727−1730.

(6) Pons-Y-Moll, O.; Perriere, J.; Millon, E.; Defourneau, R. M.; Defourneau, D.; Vincent, B.; Essahlaoui, A.; Boudrioua, A.; Seiler, W. Structural and Optical Properties of Rare-Earth-Doped Y$_2$O$_3$ Waveguides Grown by Pulsed-Laser Deposition. *J. Appl. Phys.* **2002**, *92*, 4885−4890.

(7) Niinistö, J.; Putkonen, M.; Niinistö, L. Processing of Y$_2$O$_3$ Thin Films by Atomic Layer Deposition from Cyclopentadienyl-Type Compounds and Water as Precursors. *Chem. Mater.* **2004**, *16*, 2953−2958.

(8) Päiväsaari, J.; Niinistö, J.; Arstila, K.; Kukli, K.; Putkonen, M.; Niinistö, L. High Growth Rate of Erbium Oxide Thin Films in Atomic Layer Deposition from (CpMe)$_3$Er and Water Precursors. *Chem. Vap. Deposition* **2005**, *11*, 415−419.

(9) Kondo, H.; Sakurai, S.; Sakashita, M.; Sakai, A.; Ogawa, M.; Zaima, S. Metal-Organic Chemical Vapor Deposition of High-

Dielectric-Constant Praseodymium Oxide Films Using a Cyclopentadienyl Precursor. *Appl. Phys. Lett.* **2010**, *96*, 012105.

(10) Goto, T.; Banal, R.; Kimura, T. Morphology and Preferred Orientation of $Y_2O_3$ Film Prepared by High-Speed Laser CVD. *Surf. Coat. Technol.* **2007**, *201*, 5776−5781.

(11) Goto, T.; Kimura, T. High-Speed Oxide Coating by Laser Chemical Vapor Deposition and Their Nano-Structure. *Thin Solid Films* **2006**, *515*, 46−52.

(12) Nelson, B. N.; Caster, A. G.; Berry, M. T. Gas-Phase Photoionization of Tris(2,2,6,6-tetramethyl-3,5-heptanedionato)-europium(III). *Chem. Phys. Lett.* **2004**, *396*, 256−260.

(13) Ow, F. P.; Berry, M. T.; May, P. S.; Zink, J. I. Wavelength Dependent Photofragmentation Patterns of Tris(2,2,6,6-tetramethyl-3,5-heptanedionato)Ln (III) (Ln = Eu, Tb, Gd) in a Molecular Beam. *J. Phys. Chem. A* **2006**, *110*, 7751−7754.

(14) Meng, Q.; Witte, R. J.; May, P. S.; Berry, M. T. Photodissociation and Photoionization Mechanisms in Lanthanide-Based Fluorinated *β*-Diketonate Metal-Organic Chemical-Vapor Deposition Precursors. *Chem. Mater.* **2009**, *21*, 5801−5808.

(15) Meng, Q.; Witte, R. J.; Gong, Y.; Day, E. L.; Chen, J.; May, P. S.; Berry, M. T. Thin Film Deposition and Photodissociation Mechanisms for Lanthanide Oxide Production from Tris(2,2,6,6-tetramethyl-3,5-heptanedionato)Ln(III) in Laser-Assisted MOCVD. *Chem. Mater.* **2010**, *22*, 6056−6064.

(16) Bitner, T. W.; Zink, J. I. Gas-Phase Photofragmentation of Tris(methyl vinyl ketone) Tungsten(0) and the Relationship to Laser-Assisted CVD of Tungsten Oxide Thin Films. *Inorg. Chem.* **2002**, *41*, 967−972.

(17) Cheon, J.; Guile, M.; Muraoka, P.; Zink, J. I. Gas Phase Photoproduction of Diatomic Metal Nitrides During Metal Nitride Laser Chemical Vapor Deposition. *Inorg. Chem.* **1999**, *38*, 2238−2239.

(18) Cheon, J.; Zink, J. I. In-Situ Gas-Phase Luminescence and Time-of-Flight Mass Spectroscopic Detection of Photofragments During Photochemical Synthesis of Copper Particles from Bis(*tert*-butylacetoacetato)Copper. *Inorg. Chem.* **2000**, *39*, 433−436.

(19) Muraoka, P.; Byun, D.; Zink, J. I. Excited States and Gas Phase Photofragmentation of Palladium and Platinum Hexafluoroacetylacetonates. *Coord. Chem. Rev.* **2000**, *208*, 193−211.

(20) Deumens, E.; Diz, A.; Longo, R.; Öhrn, Y. Time-Dependent Theoretical Treatments of the Dynamics of Electrons and Nuclei in Molecular Systems. *Rev. Mod. Phys.* **1994**, *66*, 917−983.

(21) Jasper, A. W.; Nangia, S.; Zhu, C.; Truhlar, D. G. Non-Born-Oppenheimer Molecular Dynamics. *Acc. Chem. Res.* **2006**, *39*, 101−108.

(22) Tully, J. C. Perspective: Nonadiabatic Dynamics Theory. *J. Chem. Phys.* **2012**, *137*, 22A301.

(23) Tully, J. C. Molecular Dynamics with Electronic Transitions. *J. Chem. Phys.* **1990**, *93*, 1061−1071.

(24) (a) Hammes-Schiffer, S.; Tully, J. C. Proton Transfer in Solution: Molecular Dynamics with Quantum Transitions. *J. Chem. Phys.* **1994**, *101*, 4657−4667. (b) Zaari, R. R.; Varganov, S. A. Nonadiabatic Transition State Theory and Trajectory Surface Hopping Dynamics: Intersystem Crossing between $^3B_1$ and $^1A_1$ States of $SiH_2$. *J. Phys. Chem. A* **2015**, *119*, 1332−1338. (c) Meek, G. A. Evaluation of the Time-Derivative Coupling for Accurate Electronic State Transition Probabilities from Numerical Simulations. *J. Phys. Chem. Lett.* **2014**, *5*, 2351−2356. (d) Makhov, D. V.; Saita, K.; Martinez, T. J.; Shalashilin, D. V. Ab Initio Multiple Cloning Simulations of Pyrrole Photodissociation: Tker Spectra and Velocity Map Imaging. *Phys. Chem. Chem. Phys.* **2015**, *17*, 3316−3325.

(25) Zhu, C.; Jasper, A. W.; Truhlar, D. G. Non-Born-Oppenheimer Liouville-Von Neumann Dynamics. Evolution of a Subsystem Controlled by Linear and Population-Driven Decay of Mixing with Decoherent and Coherent Switching. *J. Chem. Theory Comput.* **2005**, *1*, 527−540.

(26) Prezhdo, O. V. Quantum Anti-Zeno Acceleration of a Chemical Reaction. *Phys. Rev. Lett.* **2000**, *85*, 4413−4417.

(27) Ashkenazi, G.; Kosloff, R.; Ratner, M. A. Photoexcited Electron Transfer: Short-Time Dynamics and Turnover Control by Dephasing, Relaxation, and Mixing. *J. Am. Chem. Soc.* **1999**, *121*, 3386−3395.

(28) Jasper, A. W.; Truhlar, D. G. Improved Treatment of Momentum at Classically Forbidden Electronic Transitions in Trajectory Surface Hopping Calculations. *Chem. Phys. Lett.* **2003**, *369*, 60−67.

(29) Micha, D. A. A Self-Consistent Eikonal Treatment of Electronic Transitions in Molecular Collisions. *J. Chem. Phys.* **1983**, *78*, 7138−7145.

(30) Micha, D. A. Density Matrix Treatment of Electronic Rearrangement. *Adv. Quantum Chem.* **1999**, *35*, 317−337.

(31) Chaban, V. V.; Fileti, E. E.; Prezhdo, O. V. Buckybomb: Reactive Molecular Dynamics Simulation. *J. Phys. Chem. Lett.* **2015**, *6*, 913−917.

(32) Albert, V. V.; Sabin, J. R.; Harris, F. E. Simulated Structure and Energetics of Endohedral Complexes of Noble Gas Atoms in Buckminsterfullerene. *Int. J. Quantum Chem.* **2007**, *107*, 3061−3066.

(33) Isayev, O.; Gorb, L.; Qasim, M.; Leszczynski, J. Ab Initio Molecular Dynamics Study on the Initial Chemical Events in Nitramines: Thermal Decomposition of CL-20. *J. Phys. Chem. B* **2008**, *112*, 11005−11013.

(34) Greenfield, M. T.; McGrane, S. D.; Bolme, C. A.; Bjorgaard, J. A.; Nelson, T. R.; Tretiak, S.; Scharff, R. J. Photoactive High Explosives: Linear and Nonlinear Photochemistry of Petrin Tetrazine Chloride. *J. Phys. Chem. A* **2015**, *119*, 4846−4855.

(35) Grimme, S. Towards First Principles Calculation of Electron Impact Mass Spectra of Molecules. *Angew. Chem., Int. Ed.* **2013**, *52*, 6306−6312.

(36) Bauer, C. A.; Grimme, S. Elucidation of Electron Ionization Induced Fragmentations of Adenine by Semiempirical and Density Functional Molecular Dynamics. *J. Phys. Chem. A* **2014**, *118*, 11479−11484.

(37) Chen, J.; Meng, Q.; Stanley May, P.; Berry, M. T.; Kilin, D. S. Time-Dependent Excited-State Molecular Dynamics of Photodissociation of Lanthanide Complexes for Laser-Assisted Metal-Organic Chemical Vapour Deposition. *Mol. Phys.* **2014**, *112*, 508−517.

(38) Chen, J.; Hochstatter, A. M.; Kilin, D.; May, P. S.; Meng, Q.; Berry, M. T. Photofragmentation of Gas-Phase Lanthanide Cyclopentadienyl Complexes: Experimental and Time-Dependent Excited-State Molecular Dynamics. *Organometallics* **2014**, *33*, 1574−1586.

(39) Hohenberg, P.; Kohn, W. Inhomogeneous Electron Gas. *Phys. Rev.* **1964**, *136*, B864−B871.

(40) Kresse, G.; Hafner, J. Ab Initio Molecular Dynamics for Liquid Metals. *Phys. Rev. B: Condens. Matter Mater. Phys.* **1993**, *47*, 558−561.

(41) Kresse, G.; Hafner, J. Ab Initio Molecular-Dynamics Simulation of the Liquid-Metal-Amorphous-Semiconductor Transition in Germanium. *Phys. Rev. B: Condens. Matter Mater. Phys.* **1994**, *49*, 14251−14269.

(42) Kresse, G.; Furthmüller, J. Efficient Iterative Schemes for Ab Initio Total-Energy Calculations Using a Plane-Wave Basis Set. *Phys. Rev. B: Condens. Matter Mater. Phys.* **1996**, *54*, 11169−11186.

(43) Kresse, G.; Furthmüller, J. Efficiency of Ab-Initio Total Energy Calculations for Metals and Semiconductors Using a Plane-Wave Basis Set. *Comput. Mater. Sci.* **1996**, *6*, 15−50.

(44) Rabi, I. I.; Ramsey, N. F.; Schwinger, J. Use of Rotating Coordinates in Magnetic Resonance Problems. *Rev. Mod. Phys.* **1954**, *26*, 167−171.

(45) Rabi, I. I. Space Quantization in a Gyrating Magnetic Field. *Phys. Rev.* **1937**, *51*, 652−654.

(46) Huang, S.; Inerbaev, T. M.; Kilin, D. S. Excited State Dynamics of $Ru_{10}$ Cluster Interfacing Anatase $TiO_2(101)$ Surface and Liquid Water. *J. Phys. Chem. Lett.* **2014**, *5*, 2823−2829.

(47) (a) Huang, S.; Kilin, D. S. Charge Transfer, Luminescence, and Phonon Bottleneck in $TiO_2$ Nanowires Computed by Eigenvectors of Liouville Superoperator. *J. Chem. Theory Comput.* **2014**, *10*, 3996−4005. (b) Gajewicz, A.; Puzyn, T.; Rasulev, B.; Leszczynska, D.; Leszczynski, J. Metal oxide nanoparticles: size-dependence of quantum-mechanical properties. *Nanosci. Nanotechnol.–Asia* **2012**, *1*

(1), 53−58. (c) Mikolajczyk, A.; Gajewicz, A.; Rasulev, B.; Schaeublin, N.; Maurer-Gardner, E.; Hussain, S.; Leszczynski, J.; Puzyn, T. Zeta Potential for Metal Oxide Nanoparticles: A Predictive Model Developed by a Nano-Quantitative Structure−Property Relationship Approach. *Chem. Mater.* **2015**, *27*, 2400−2407.

(48) (a) Mavros, M. G.; Micha, D. A.; Kilin, D. S. Optical Properties of Doped Silicon Quantum Dots with Crystalline and Amorphous Structures. *J. Phys. Chem. C* **2011**, *115*, 19529−19537. (b) Kryjevski, A.; Kilin, D. Multiple Exciton Generation in Silicon Quantum Dot Arrays: Density Functional Perturbation Theory Computation. *Mol. Phys.* **2014**, *112*, 430−440.

(49) Kilin, D. S.; Tsemekhman, K. L.; Kilina, S. V.; Balatsky, A. V.; Prezhdo, O. V. Photoinduced Conductivity of a Porphyrin−Gold Composite Nanowire. *J. Phys. Chem. A* **2009**, *113*, 4549−4556.

(50) (a) Chen, J.; Schmitz, A.; Inerbaev, T.; Meng, Q.; Kilina, S.; Tretiak, S.; Kilin, D. S. First-Principles Study of p-n-Doped Silicon Quantum Dots: Charge Transfer, Energy Dissipation, and Time-Resolved Emission. *J. Phys. Chem. Lett.* **2013**, *4*, 2906−2913. (b) Kilina, S.; Kilin, D.; Tretiak, S. Light-Driven and Phonon-Assisted Dynamics in Organic and Semiconductor Nanostructures. *Chem. Rev.* **2015**, *115*, 5929−5978.

(51) Goyal, P.; Schwerdtfeger, C. A.; Soudackov, A. V.; Hammes-Schiffer, S. Nonadiabatic Dynamics of Photoinduced Proton-Coupled Electron Transfer in a Solvated Phenol−Amine Complex. *J. Phys. Chem. B* **2015**, *119*, 2758−2768.

(52) Auer, B.; Soudackov, A. V.; Hammes-Schiffer, S. Nonadiabatic Dynamics of Photoinduced Proton-Coupled Electron Transfer: Comparison of Explicit and Implicit Solvent Simulations. *J. Phys. Chem. B* **2012**, *116*, 7695−7708.

(53) Nguyen, T. S.; Nanguneri, R.; Parkhill, J. How Electronic Dynamics with Pauli Exclusion Produces Fermi−Dirac Statistics. *J. Chem. Phys.* **2015**, *142*, 134113.

(54) Nguyen, T. S.; Parkhill, J. Nonadiabatic Dynamics for Electrons at Second-Order: Real-Time TDDFT and OSCF2. *J. Chem. Theory Comput.* **2015**, *11*, 2918−2924.

(55) (a) Redfield, A. G. On the Theory of Relaxation Processes. *IBM J. Res. Dev.* **1957**, *1*, 19−31. (b) Kilin, D. S.; Micha, D. A. Relaxation of photoexcited electrons at a nanostructured Si (111) surface. *J. Phys. Chem. Lett.* **2010**, *1*, 1073−1077. (c) Trinastic, J. P.; Chu, I.-H.; Cheng, H.-P. Manipulating the Phonon Bottleneck in Graphene Quantum Dots: Phonon-Induced Carrier Relaxation within the Linear Response Theory. *J. Phys. Chem. C* **2015**, *119* (39), 22357−22369.

(56) Han, Y.; Tretiak, S.; Kilin, D. Dynamics of Charge Transfer at Au/Si Metal-Semiconductor Nano-Interface. *Mol. Phys.* **2014**, *112*, 474−484.

(57) Han, Y.; Micha, D. A.; Kilin, D. S. Ab Initio Study of the Photocurrent at the Au/Si Metal−Semiconductor Nanointerface. *Mol. Phys.* **2015**, *113*, 327−335.

(58) Derricotte, W. D.; Evangelista, F. A. Simulation of X-Ray Absorption Spectra with Orthogonality Constrained Density Functional Theory. *Phys. Chem. Chem. Phys.* **2015**, *17*, 14360−14374.

(59) Jeffcoat, D. B.; DePrince, A. E. N-Representability-Driven Reconstruction of the Two-Electron Reduced-Density Matrix for a Real-Time Time-Dependent Electronic Structure Method. *J. Chem. Phys.* **2014**, *141*, 214104.

(60) Evangelista, F. A. A Driven Similarity Renormalization Group Approach to Quantum Many-Body Problems. *J. Chem. Phys.* **2014**, *141*, 054109.

(61) Akimov, A. V.; Neukirch, A. J.; Prezhdo, O. V. Theoretical Insights into Photoinduced Charge Transfer and Catalysis at Oxide Interfaces. *Chem. Rev.* **2013**, *113*, 4496.

(62) Stier, W.; Prezhdo, O. V. Nonadiabatic Molecular Dynamics Simulation of Light-Induced, Electron Transfer from an Anchored Molecular Electron Donor to a Semiconductor Acceptor. *J. Phys. Chem. B* **2002**, *106*, 8047−8054.

(63) Humphrey, W.; Dalke, A.; Schulten, K. VMD: Visual Molecular Dynamics. *J. Molec. Graphics* **1996**, *14*, 33−38.

(64) *Jmol: an open-source Java viewer for chemical structures in 3D.* http://www.jmol.org/.